Industrial Chemistry & Materials

ROYAL SOCIETY OF CHEMISTRY

PAPER

View Article Online
View Journal | View Issue

Cite this: *Ind. Chem. Mater.*, 2026, **4**, 105

Integrated CO_2 capture and methane dry reforming over a Ni–Ca dual functional material under SO_2/NO_2-containing flue gas conditions: a mechanistic study

Bocheng Yu,[a] Muqing Yang,[a] Yijian Qiao,[a] Yaozu Wang,[a] Yongqing Xu,[a] Xuan Bie,[a] Qinghai Li,[a] Yanguo Zhang,[a] Shuzhuang Sun*[b] and Hui Zhou *[ac]

Received 24th May 2025,
Accepted 27th June 2025

DOI: 10.1039/d5im00087d

rsc.li/icm

Integrated carbon capture and utilization (ICCU) has emerged as a promising strategy toward carbon neutrality. However, most existing studies rely on simulated flue gas compositions, neglecting the impact of common impurities such as sulfur oxides (SO_x) and nitrogen oxides (NO_x), thereby limiting the practical industrial applicability of ICCU technologies. Herein, we systematically investigate the effects of SO_2 and NO_2 at various concentrations on the adsorption–catalysis performance based on a representative Ni–Ca dual functional material (DFM) in the ICCU–dry reforming of methane (ICCU-DRM) process. Exposure to 100 ppm SO_2 showed a negligible influence on catalytic activity but markedly inhibited carbon deposition. Further increasing the SO_2 concentration to 500 ppm led to complete deactivation of the DFM. NO_2 exhibited a similar concentration-dependent trend to SO_2, albeit with a comparatively lower impact. Mechanistic analysis revealed that both SO_2 and NO_2 promote the formation of a coating layer of calcium-containing compounds on the surface of Ni nanoparticles, accounting for the partial or total deactivation. These findings offer critical insights into the industrial applications of ICCU systems under realistic flue gas conditions.

Keywords: Integrated carbon capture and utilization; SO_x and NO_x; Deactivation; Phase transition; DRM.

1 Introduction

Excessive anthropogenic CO_2 emissions are causing severe global warming, leading to the frequent occurrence of extreme weather.[1,2] Carbon capture, utilization and storage (CCUS) are believed as one of the most promising ways to achieve net zero by this mid-century as an industrial-level technology.[3–5] Compared to carbon capture and storage (CCS), carbon capture and utilization (CCU) can convert the captured CO_2 into high-value chemical products (CO, CH_4, CH_3OH, *etc.*), which shows a better economy with the avoidance of carbon leaks. Among most of the C1 production reactions (reverse water gas shift, methanation, *etc.*), dry reforming of methane (DRM, eqn (1)) can simultaneously convert two main greenhouse gases CH_4 and CO_2 into syngas, which serves as a feedstock for other important chemical reactions like methanol production and Fischer–Tropsch synthesis.[6,7] However, high CO_2 storage and transportation costs and massive energy consumption in temperature and pressure swing operations severely restrain the wide deployment of CCU technologies.[8,9]

$$CO_2 + CH_4 \rightarrow 2CO + 2H_2 \quad \Delta H = +274\ \text{kJ mol}^{-1} \qquad (1)$$

Recently, by combining the CO_2 capture and chemical utilization into one reactor, integrated carbon capture and utilization (ICCU) has gained increasing interest from researchers and engineers.[10–14] To achieve these two processes in one reactor, dual function materials (DFMs), consisting of an adsorptive component for carbon capture and a catalytic component for carbon conversion, are crucial to achieve high performance ICCU processes.[15–18] Since DRM is a strongly endothermic reaction and needs high temperature conditions (600–900 °C), Ca-based sorbents are the most promising candidates for carbon capture.[19,20] However, Ca-based sorbents severely suffer from sintering, leading to a sharply decreased CO_2 capacity after cycles.[21,22] Thus, promoters including MgO, Al_2O_3 and ZrO_2 are

[a] *Key Laboratory for Thermal Science and Power Engineering of Ministry of Education, Beijing Key Laboratory of CO_2 Utilization and Reduction Technology, Department of Energy and Power Engineering, Tsinghua University, Beijing 100084, P.R. China. E-mail: huizhou@tsinghua.edu.cn*
[b] *School of Chemical Engineering, Zhengzhou University, Zhengzhou 450001, P.R. China. E-mail: ssun@zzu.edu.cn*
[c] *Shanxi Research Institute for Clean Energy, Tsinghua University, Taiyuan, Shanxi 030000, P.R. China*

commonly introduced into DFMs to enhance the CaO stability by acting as the physical barrier.[23–25] Ni as an earth-abundant metal, showing excellent catalytic activity to methane activation, has become one of the most impressive choices for the catalytic components.[26–28]

Previous studies focused on the outperformed DFM design and adsorptive–catalytic mechanism investigation *via* ideal flue gas (a mixture of CO_2 and N_2), while few studies investigated the influence of impurity components in the realistic flue gas. SO_x and NO_x, as two of the most important pollutants in flue gas, have been proven to significantly influence the capture and conversion performance.[29–31] Previous studies reported that SO_2 and NO_2 could poison CO_2 hydrogenation catalysts, primarily attributed to the strong chemisorption of intermediate species on active metal sites or generation of stable metal sulfides which irreversibly block active sites.[32,33] Also, as an alkaline sorbent, CaO can adsorb acidic SO_2 and NO_2, affecting its adsorptive performance.[34,35] Notably, as for the ICCU-DRM process, the reaction atmosphere frequently switches between an oxidizing atmosphere (CO_2/N_2) and a reductive atmosphere (CH_4/N_2), which brings new understandings compared to independent capture or conversion scenarios.

Herein, we investigated the influence of SO_2 and NO_2 on typical Ni–Ca DFMs. The Ni5Al15Ca DFM as a representative DFM for ICCU-DRM was synthesized by sol–gel methods, in which Ni provides high catalytic activity, CaO captures CO_2 in flue gas and Al_2O_3 acts as a stabilizer. A series of tests at different SO_2 and NO_2 concentrations were performed to uncover the influence of these pollutants in flue gas. A low concentration of SO_2 (100 ppm) in flue gas showed a negligible influence on catalytic activity but markedly reduced the H_2:CO ratio. Further increasing the SO_2 concentration to 500 ppm resulted in complete deactivation of the DFM. NO_2 showed a similar phenomenon to SO_2 with a comparatively lower impact. Systematic characterization was performed and revealed the formation of a coating layer on the surface of Ni nanoparticles induced by SO_2 and NO_2, accounting for the partial or total deactivation. This study aims to offer critical insights into the industrial applications of ICCU systems under realistic flue gas conditions.

2 Results and discussion

2.1 Performance evaluation of the SO_2 and NO_2 influence

The impact of SO_2 and NO_2 in flue gas on the performance of ICCU-DRM was evaluated through a series of tests at varying SO_2 and NO_2 concentrations (100, 200, and 500 ppm). Without SO_2 or NO_2 in flue gas, the performance of the Ni5Al15Ca DFM was first assessed in the absence of SO_2 and NO_2. The real-time concentrations of CO_2, CO, H_2, and CH_4 during the first and second cycles are shown in Fig. 1. During the CO_2 capture stage, CO_2 was adsorbed by CaO, accompanied by CO formation attributed to the reverse Boudouard reaction ($CO_2 + C \rightarrow 2CO$) from the second cycle. The elevated CO amount indicated the severe carbon

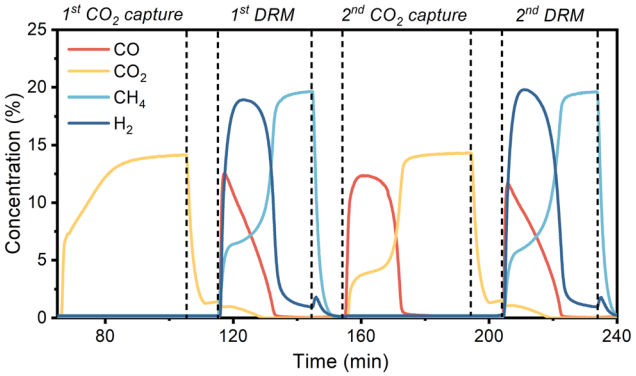

Fig. 1 Real-time gas concentrations of ICCU-DRM for the first and second cycles.

deposition during the previous dry reforming stage. In the subsequent dry reforming stage, CH_4 reacted with the captured CO_2 to produce CO and H_2. Simultaneously, CH_4 could decompose into carbon and H_2 as a common side reaction. Notably, although CO was no longer detected at the final dry reforming stage, H_2 remained generated, highlighting the strong CH_4 decomposition activity of Ni sites.

The cyclic performance of the Ni5Al15Ca DFM was systematically evaluated, as illustrated in Fig. 2. CO_2 conversion as a primary indicator of catalytic efficiency reached 81.3% in the first cycle and exhibited only a slight decline to 76.3% after 10 cycles (Fig. 2a). The results confirm the high activity and stability of the Ni active sites to the dry reforming process. Despite the CO_2 conversion, the H_2:CO ratio was notably higher than the ideal stoichiometric value of 1, reaching 2.39 in the first cycle (Fig. 2b). This deviation suggests the occurrence of CH_4 decomposition as a side reaction, which contributes to excess hydrogen production and promotes carbon deposition on the catalyst surface. The elevated carbon accumulation was further evidenced by the CO yield during the carbonation stage (Fig. 2d). Notably, the CO_2 capacity of Ni5Al15Ca remained relatively stable over the 10 cycles, only decreasing from 10.9 to 9.5 mmol g^{-1} (Fig. 2c). Such stability is attributed to the presence of Al_2O_3, which can act as a physical barrier during cycles.

The influence of varying SO_2 concentrations (100, 200, and 500 ppm) on the performance of the Ni5Al15Ca DFM was investigated. As shown in Fig. 2a, under 100 ppm SO_2 conditions, the DFM reached a CO_2 conversion of 79.4% in the 10th cycle, even slightly higher than the SO_2-free DFM. However, as for 200 ppm SO_2, a significant decline in CO_2 conversion was observed over the cycles, with CO_2 conversion dropping to just 37.4% for the 10th cycle. Further increasing the SO_2 concentration to 500 ppm resulted in severe deactivation, with CO and H_2 becoming undetectable in the 10th cycle. Results demonstrate that low SO_2 concentrations show negligible impact on the CO_2 conversion performance, while higher concentrations lead to significant DFM deactivation for ICCU-DRM.

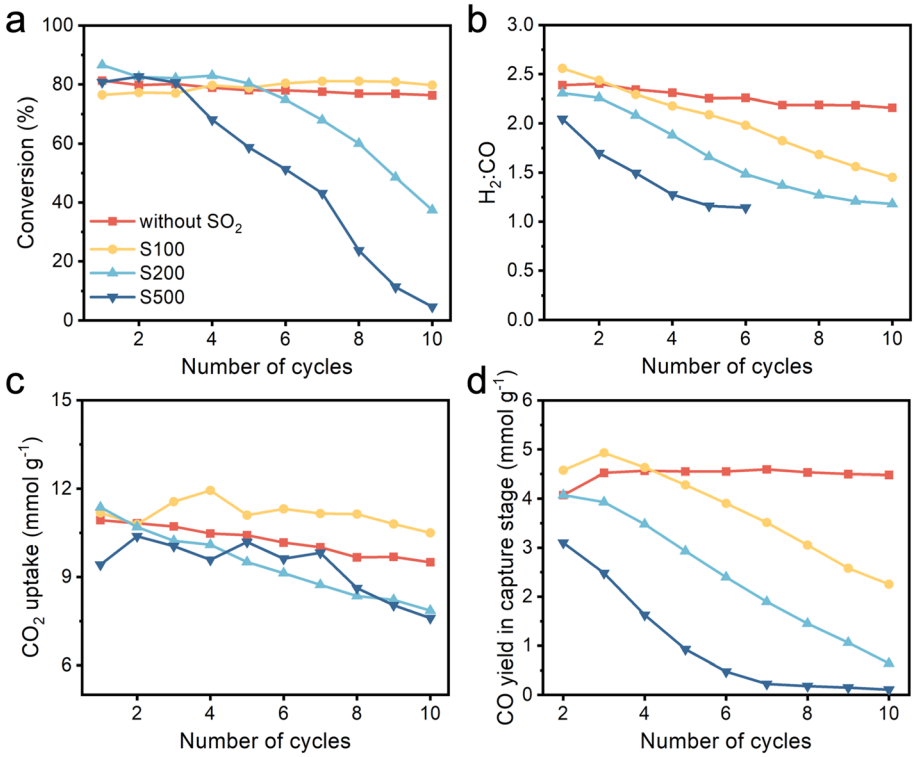

Fig. 2 Cyclic performance of ICCU-DRM under SO_2-containing flue gas conditions. (a) CO_2 conversion, (b) H_2 : CO ratio, (c) CO_2 uptake and (d) CO yield in the capture stage. S100 refers to the cycled DFM with 100 ppm SO_2 in flue gas.

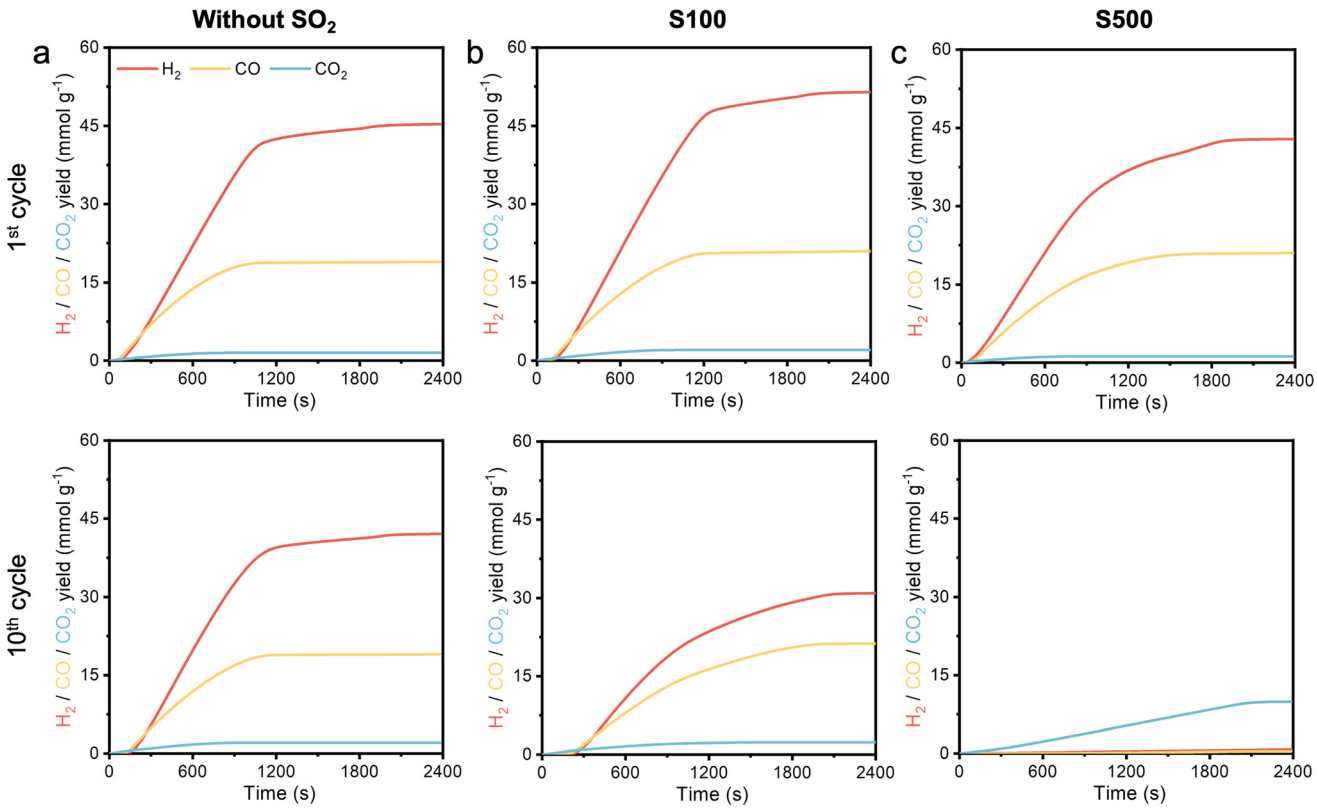

Fig. 3 Real-time gas concentrations with SO_2-containing flue gas of ICCU-DRM for the 1st and 10th cycles. (a) Without SO_2 or NO_2 in flue gas, (b) 100 ppm SO_2-containing flue gas, and (c) 500 ppm SO_2-containing flue gas.

The H_2:CO ratio as another key performance indicator was also examined, as presented in Fig. 2b. Interestingly, under 100 ppm SO_2 conditions, the H_2:CO ratio gradually decreased over the cycles and approached the ideal stoichiometric value of 1, and a similar but more significant trend can be observed under 200 ppm SO_2 conditions. The results suggest that SO_2 in flue gas can suppress the CH_4 decomposition side reaction, thereby mitigating carbon deposition. The decreased carbon deposition could further be supported by the decreased CO yield during the subsequent carbonation stage (Fig. 2d). Since both CO and H_2 production diminished to near-zero levels after the 6th cycle under 500 ppm SO_2 conditions, the H_2:CO ratio was irrelevant in the final 4 cycles. Notably, the absence of CO during the carbonation stage under 500 ppm SO_2 conditions also suggested that no carbon deposition occurred. Collectively, these findings indicate that SO_2 can reduce carbon deposition and improve product selectivity for the dry reforming process.

The observed differences in the CO_2 conversion and H_2:CO ratio between SO_2-containing and SO_2-free conditions can be attributed to the different reaction kinetics. Thus, the real-time gas concentrations for the 1st and 10th cycles are presented in Fig. 3. For the Ni5Al15Ca DFM under SO_2-free conditions, negligible differences were observed between the 1st and 10th cycles, suggesting that the Ni active sites remained catalytically stable for both methane dry reforming and methane decomposition. However, after introducing low concentrations of SO_2 to the DFM, a rapid catalytic activity loss was observed, evidenced by the slower formation of both CO and H_2. SO_2 exhibited a more pronounced inhibitory effect on the CH_4 decomposition than on the dry reforming reaction, resulting in relatively unchanged CO_2 conversion but a significantly decreased H_2:CO ratio. This shift indicates suppression of the side reaction responsible for excess methane consumption and carbon deposition. At higher SO_2 concentrations, however, the CO_2 conversion itself became adversely affected, resulting in nearly complete deactivation.

Furthermore, the effect of SO_2 on the cyclic stability of CO_2 capture by the Ni5Al15Ca DFM was assessed, as shown in Fig. 2c. Under 100 ppm SO_2 conditions, the initial CO_2 uptake was comparable to the SO_2-free conditions. Notably, Ni5Al15Ca even exhibited an improved capacity retention under such conditions, with only a 6.1% decrease after 10 cycles, compared to the 13.6% decrease observed in the DFM without SO_2 or NO_2. Enhanced stability could be attributed to the formation of thermally stable species such as CaS and $CaSO_4$ (*vide infra*), which could act as physical barriers to suppress the CaO sintering. However, increasing SO_2 concentrations led to decreased CO_2 uptake with cycling. Such deactivation was likely due to the continuous formation of CaS and $CaSO_4$, consuming active CaO components and thereby reducing the theoretical CO_2 capacity of the DFM. In short, while limited formation of these sulfur-containing phases may enhance stability by serving as physical barriers,

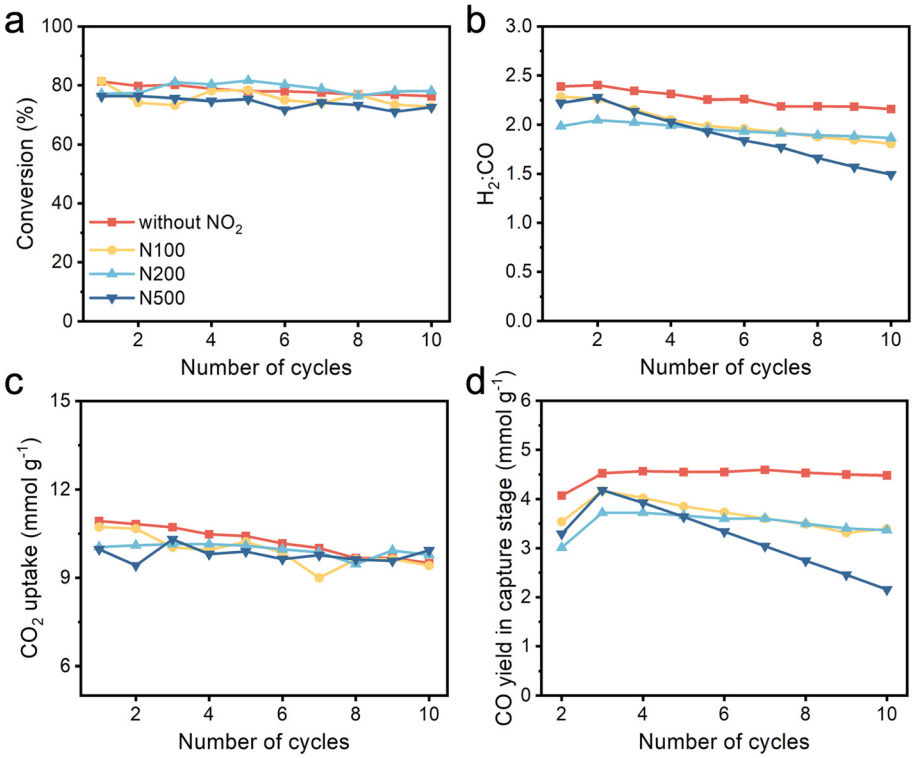

Fig. 4 Cyclic performance of ICCU-DRM under NO_2-containing flue gas conditions. (a) CO_2 conversion, (b) H_2:CO ratio, (c) CO_2 uptake and (d) CO yield in the capture stage. N100 refers to the cycled DFM with 100 ppm NO_2 in flue gas.

excessive accumulation compromises the sorbent capacity until equilibrium is reached.

The influence of NO_2 in the flue gas was further investigated, as shown in Fig. 4. Similar to SO_2, NO_2 induced a similar CO_2 conversion but a shift in the H_2:CO ratio; however, its impact was significantly less severe. Notably, the Ni5Al15Ca DFM retained considerable catalytic activity even under 500 ppm NO_2 conditions, whereas complete deactivation occurred at the same concentration of SO_2. These differences can be attributed to the relatively milder deactivation of Ni active sites by NO_2, as compared to SO_2, for both dry reforming and methane decomposition reactions (Fig. 5). In addition, NO_2 had a minimal effect on CO_2 uptake capacity, likely because nitrogen species do not accumulate within the DFM (*vide supra*). Overall, while NO_2 exhibits a similar mode of influence to SO_2, its detrimental effects are significantly less pronounced.

2.2 Mechanism study of the SO_2 and NO_2 influences

To elucidate the performance impacts of SO_2 and NO_2, a series of systematic characterization studies were conducted to reveal the underlying mechanisms. The elemental composition of the as-synthesized Ni5Al15Ca material, determined by inductively coupled plasma optical emission spectroscopy (ICP-OES), is summarized in Table 1. X-ray diffraction (XRD) (Fig. 6a) indicated that the pre-reduced Ni5Al15Ca was primarily composed of CaO (PDF# 96-900-8606) and metallic Ni (PDF# 96-151-2527), while Al existed in an amorphous phase. Scanning electron microscopy (SEM) revealed that the pre-reduced Ni5Al15Ca DFM possessed a porous morphology (Fig. 6b), and transmission electron microscopy (TEM) further confirmed the dispersion of Ni nanoparticles on the blocky CaO support (Fig. 6c). N_2 physisorption measurements (Fig. 6d) showed a specific surface area of 13.4 $m^2\ g^{-1}$ with an average pore diameter of 23.6 nm, indicative of a mesoporous structure of the DFM. H_2 temperature-programmed reduction (H_2-TPR) analysis (Fig. 6e) demonstrated the reducibility of NiO or Ni–Al spinel species to metallic Ni under H_2, which was consistent with the XRD and TEM observations. The CO_2 uptake capacity of the pre-reduced DFM was measured to be 10.4 mmol g^{-1} by thermal gravimetric analysis (TGA), in good agreement with the results obtained from the fixed-bed reactor experiments (Fig. 6f).

Table 1 Elementary analysis of pre-reduced and cycled DFMs

DFM	Ni[a] (%)	Al (%)	Ca (%)	S (%)
Pre-reduced	5.1	6.6	57.1	—
Cycled-S100	4.2	6.0	45.6	1.6
Cycled-S500	4.1	5.8	44.5	5.9

[a] Mass ratio of Ni, Al, Ca and S was tested by ICP-OES.

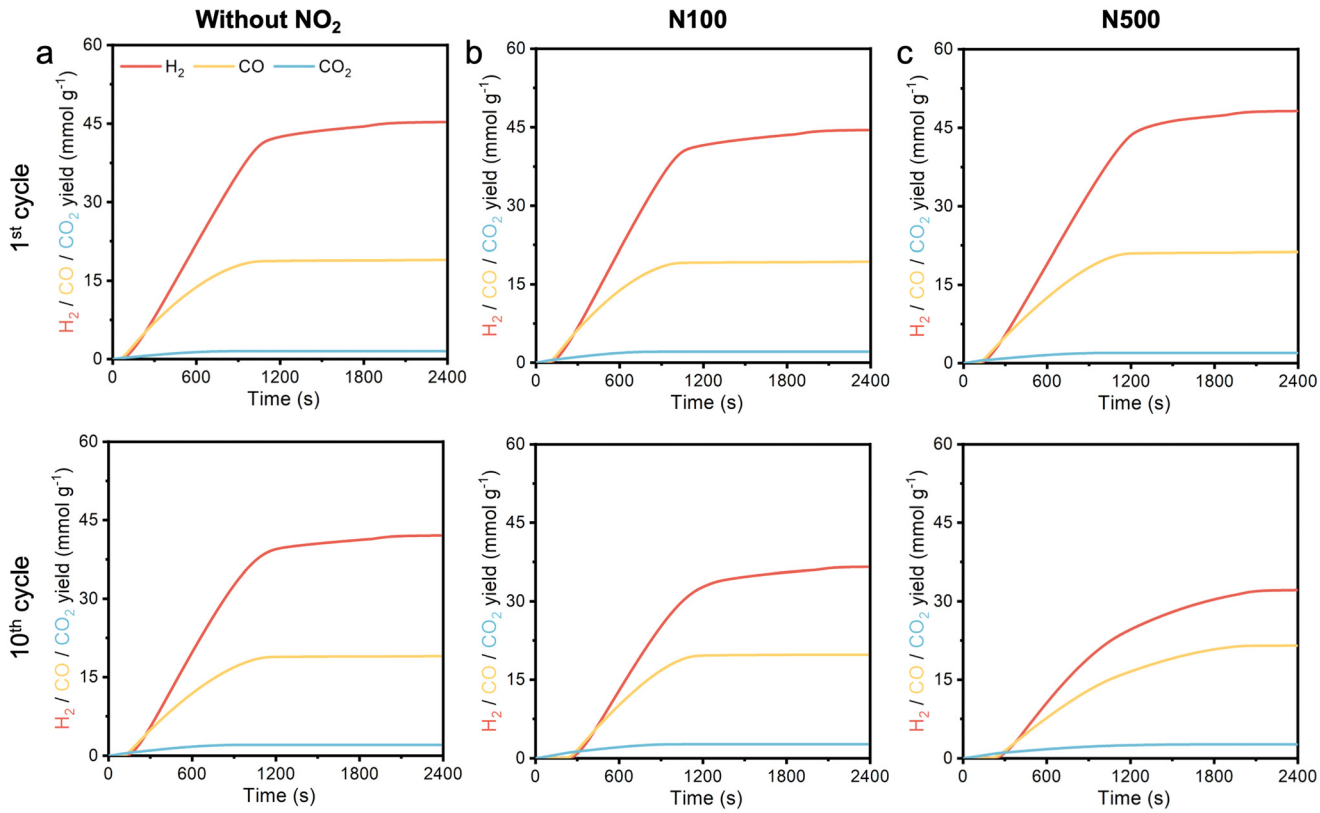

Fig. 5 Real-time gas concentrations with NO_2-containing flue gas of ICCU-DRM for the 1st and 10th cycles. (a) Without SO_2 or NO_2 in flue gas, (b) 100 ppm NO_2-containing flue gas, and (c) 500 ppm NO_2-containing flue gas.

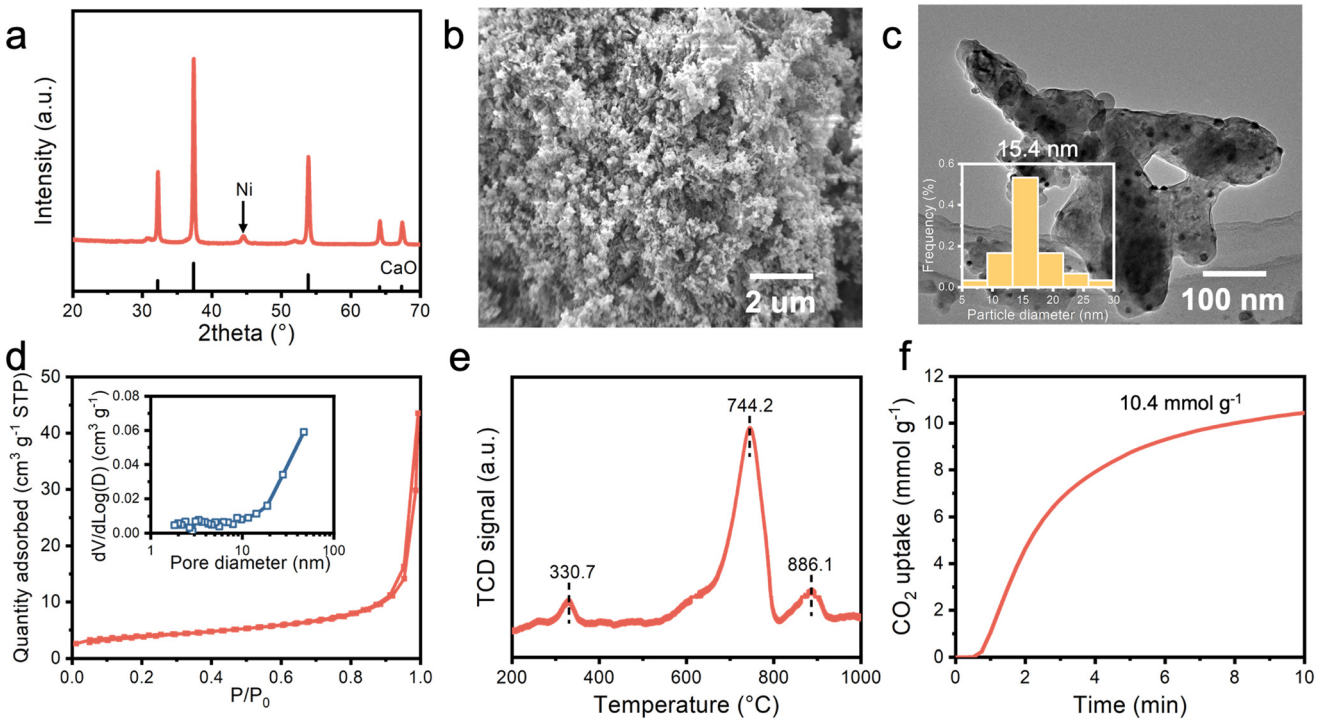

Fig. 6 Characteristics of the pre-reduced Ni5Al15Ca dual functional material. (a) XRD pattern of the pre-reduced DFM, (b) SEM image of the pre-reduced DFM, (c) TEM image of the pre-reduced DFM (inset: particle diameter distribution), (d) surface area of the pre-reduced DFM (inset: pore diameter distribution of the pre-reduced DFM), (e) H_2-TPR curve of the calcined DFM and (f) TGA curve of the pre-reduced DFM.

The crystal structures of the cycled Ni5Al15Ca DFMs were analyzed by XRD, as shown in Fig. 7. After 10 cycles under SO_2- and NO_2-free conditions, the characteristic phases of CaO and metallic Ni remained detectable, although the significant decrease in peak intensity was attributed to the formation of amorphous carbon deposits. When cycled in flue gas containing SO_2, new diffraction peaks corresponding to CaS (PDF# 96-900-8607) appeared at both 100 ppm and 500 ppm SO_2 concentrations, whereas a minor $CaSO_4$ (PDF# 96-900-4097) phase was only observed for 500 ppm SO_2. The accumulation of sulfur species after 10 cycles in SO_2-containing atmospheres was further confirmed by ICP-OES. Given the relative stability of $CaSO_4$ and CaS under dry reforming conditions, the sulfur content reached approximately 1.6% and 5.9% for the 100 ppm and 500 ppm SO_2 cases, respectively (Table 1). However, for the samples exposed to NO_2-containing flue gas, only CaO and Ni phases were detected by XRD. Notably, higher NO_2 concentrations corresponded to increased peak intensities, consistent with the suppression of carbon deposition (*vide supra*). Elemental analysis showed no detectable nitrogen in the cycled DFM, indicating that nitrogen species did not accumulate during methane dry reforming.

Given the significant impact of SO_2 on the crystal phase change of the DFM, *in situ* XRD was conducted to elucidate the dynamic phase transformations during the carbonation and dry reforming stages (Fig. 8). Upon

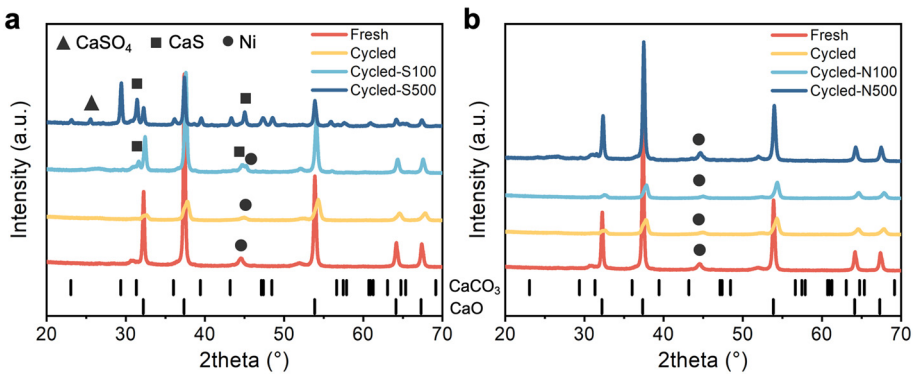

Fig. 7 XRD patterns of pre-reduced and cycled DFMs. (a) SO_2-containing and (b) NO_2-containing flue gas.

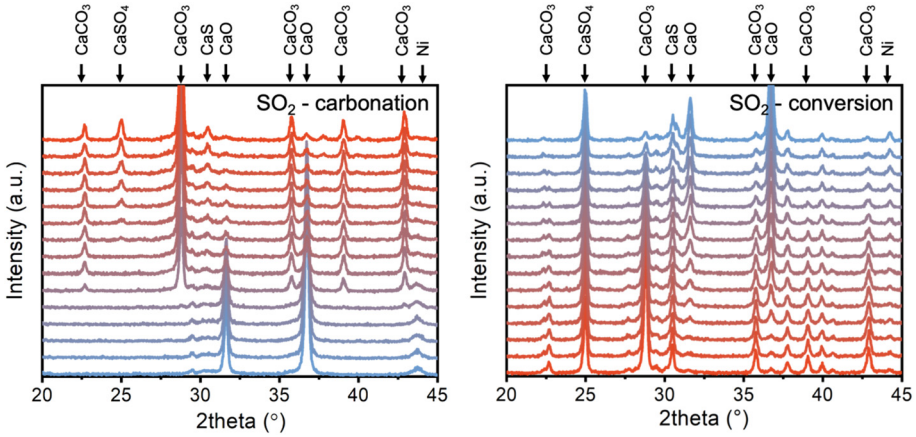

Fig. 8 *In situ* XRD patterns of ICCU-DRM under SO_2-containing flue gas conditions. Each scan continued for 2.5 min.

introduction of SO_2-containing flue gas into the reactor, the characteristic CaO peaks gradually diminished concurrent with the emergence of $CaCO_3$ peaks (PDF# 96-900-0967), confirming effective CO_2 capture. Notably, $CaSO_4$ was detected at the onset of the carbonation stage, reflecting the adsorption of SO_2 by the CaO sorbent. As the reaction progressed, CaS formation could be observed, likely resulting from the disproportionation of SO_2 (eqn (2)). During the conversion stage, in addition to the decomposition of $CaCO_3$ regenerating CaO, an increase in CaS peak intensity accompanied by a decrease in $CaSO_4$ peak intensity was detected. This trend is consistent with the reduction of $CaSO_4$ by CH_4 to form CaS (eqn (3)).[36]

$$4CaO + 4SO_2 \rightarrow 3CaSO_4 + CaS \quad \Delta H = -1059\ \text{kJ mol}^{-1} \quad (2)$$

$$CH_4 + CaSO_4 \rightarrow CO_2 + CaS + 2H_2O \quad \Delta H = +162\ \text{kJ mol}^{-1} \quad (3)$$

The surface morphologies of the cycled DFMs are shown in Fig. 9. Severe pore collapse was observed after cycling, suggesting that the Ni5Al15Ca DFM underwent significant sintering. Notably, no discernible morphological differences could be observed between DFMs cycled in SO_2- or NO_2-containing atmospheres and without SO_2 or NO_2 conditions, indicating that SO_2 and NO_2 had a minimal influence on the surface morphology. However, both SO_2 and NO_2 exhibited clear effects on the pore structure, as evidenced by N_2 physisorption analysis (Fig. 10 and Table 2). Compared with the pre-reduced DFM, most cycled samples, except for the DFM exposed to 500 ppm SO_2, exhibited an increase in surface area, primarily due to carbon deposition. Prior studies have shown that sintering of CaO-based DFMs typically results in a decreased pore diameter due to the collapse of macropores. In the presence of SO_2, the average pore diameter increased to 24.2 nm and 33.0 nm (at 100 ppm and 200 ppm, respectively), in contrast to the 16.8 nm

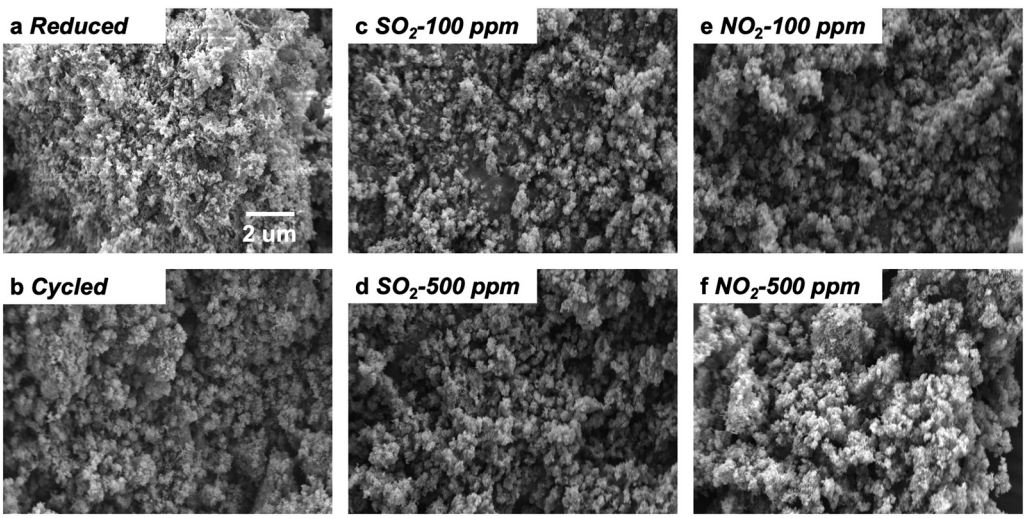

Fig. 9 SEM images of pre-reduced and cycled Ni5Al15Ca DFMs. (a) Pre-reduced DFM, (b) cycled DFM without SO_2 or NO_2, (c) cycled DFM with 100 ppm SO_2-containing flue gas, (d) cycled DFM with 500 ppm SO_2-containing flue gas, (e) cycled DFM with 100 ppm NO_2-containing flue gas, and (f) cycled DFM with 500 ppm NO_2-containing flue gas.

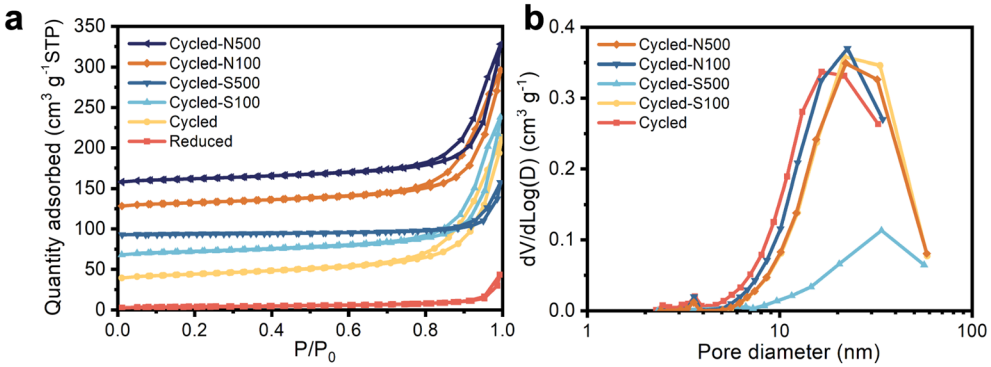

Fig. 10 N_2 physisorption of cycled DFMs. (a) BET surface area and (b) pore diameter distribution.

observed in the SO_2-free cycled DFM. The increased pore diameter was likely due to the formation of CaS and $CaSO_4$, as confirmed by XRD. Sulfur-containing species were ascribed to the increased Tammann temperatures, which function as physical barriers to effectively suppress CaO sintering. Interestingly, a similar trend could be observed in the NO_2-containing case, despite the absence of stable nitrogen-containing crystal phases. The increase in pore diameter for the NO_2-treated DMF was hypothesized to result from pore generation during the decomposition of transient calcium nitrite intermediates.

The Ni nanoparticles and elemental distribution were further examined by TEM equipped with energy-dispersive X-ray analysis (EDX), as shown in Fig. 11. The pre-reduced and cycled DFMs exhibited similar Ni nanoparticle size, indicating that sintering played a minor role in deactivation of Ni active sites. After 10 cycles without SO_2 or NO_2, carbon nanotubes (CNTs) were observed, originating from carbon deposition during CH_4 decomposition. Under 100 ppm SO_2 conditions, the morphology of Ni nanoparticles remained unchanged, indicating that low-concentration SO_2 exhibited a minimal influence on the nanostructure. However, at elevated SO_2 concentration (500 ppm), CNTs were no longer observed, which was consistent with the reduced carbon deposition observed in fixed-bed reactor tests. Line-scan EDX analysis revealed a strong spatial correlation between sulfur and nickel signals (Fig. 11c), even though no NiS phases were detected by XRD. Close-up lattice-resolved imaging further confirmed the presence of NiS by identifying lattice fringes with a spacing of 0.322 nm, corresponding to the (111) crystal plane of NiS. These results suggest that sulfur, likely in the form of CaS or NiS, coated the surface of Ni nanoparticles, leading to blockage of active sites and consequent catalytic deactivation. In the case of NO_2-containing flue gas, a similar nanoparticle morphology was observed, while the N element was undetectable in the EDX, in agreement with bulk elemental analysis. Although NO_2 did not leave a residual nitrogen species on the DFM after cycling, TEM images (Fig. 11e) revealed a distinct coating layer of CaO. This could be attributed to the acidic nature of NO_2, which likely promotes surface restructuring of the alkaline CaO, resulting in the formation of a coating layer.

Table 2 BET surface area and averaged pore diameter of pre-reduced and cycled DFMs

DFM	BET surface (m^2 g^{-1})	Averaged pore diameter[a] (nm)
Pre-reduced	13.4	23.6
Cycled	49.6	16.8
Cycled-S100	42.0	24.2
Cycled-S500	13.0	33.0
Cycled-N100	44.5	18.9
Cycled-N500	41.8	24.2

[a] The pore diameter was calculated from the BJH desorption branch ($4V/A$).

The nature and structure of carbon deposits on the cycled Ni5Al15Ca DFMs were further examined by Raman spectroscopy, as shown in Fig. 12. The DFM cycled without SO_2 or NO_2 exhibited two prominent peaks centered at approximately 1357 cm^{-1} (D band) and 1579 cm^{-1} (G band), corresponding to amorphous carbon and graphitic sp^2 carbon, respectively. The intensity ratio (I_D/I_G) was used to evaluate the degree of graphitization. In the absence of SO_2 and NO_2, the cycled DFM displayed an I_D/I_G value of 1.1, indicative of the formation of highly graphitic carbon structures such as carbon nanotubes, consistent with TEM observations. Upon exposure to 100 ppm SO_2, the I_D/I_G ratio increased to 1.6, likely due to partial deactivation of Ni active sites. For the DFM exposed to 500 ppm SO_2, neither D nor G bands were detectable, indicating the absence of detectable carbon deposition, which was consistent with the TEM and reactor data. Introduction of NO_2 during the CO_2 capture stage showed a minimal effect on the type of carbon formed during the CH_4 dry reforming step. However, carbon deposition was evidently suppressed, as corroborated by fixed-bed reactor results, even though the Raman spectra did not indicate significant changes in the graphitization degree.

X-ray photoelectron spectroscopy (XPS) was conducted to gain insight into the surface elemental composition and chemical states of the cycled Ni5Al15Ca DFMs, as shown in Fig. 13. Sulfur species were clearly detected on the surface after exposure to 100 ppm SO_2, with significantly intensified

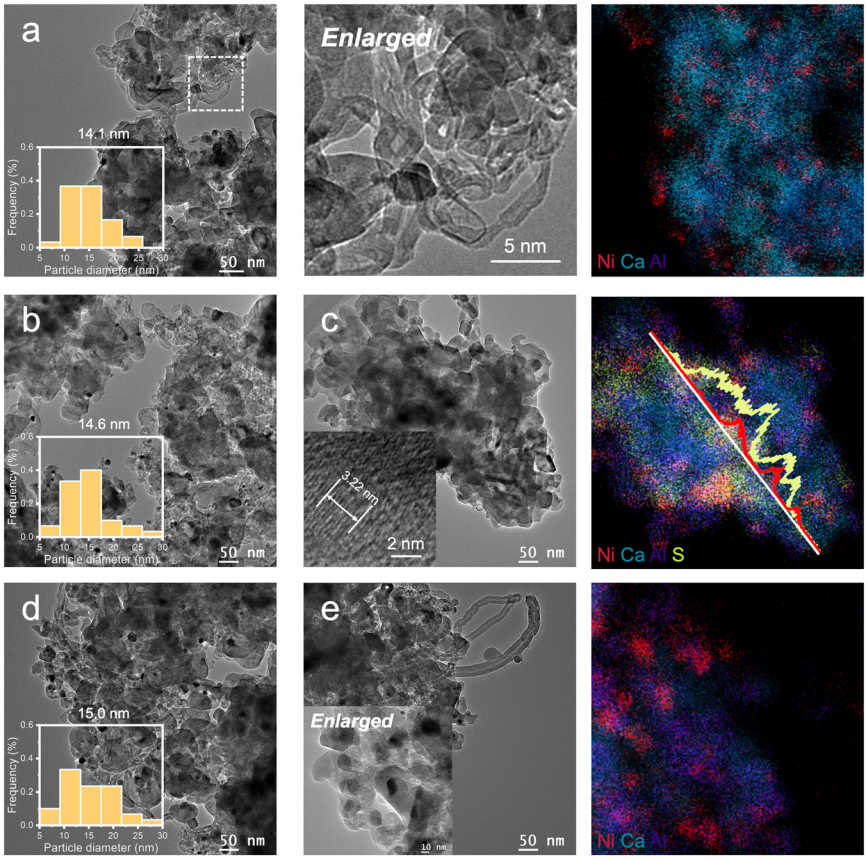

Fig. 11 TEM images of cycled DFMs. (a) Cycled DFM with enlarged CNTs and EDX (inset: particle diameter distribution), (b) cycled DFM with 100 ppm SO_2-containing flue gas (inset: particle diameter distribution), (c) cycled DFM with 500 ppm SO_2-containing flue gas and EDX (inset: close-up lattice-resolved image), (d) cycled DFM with 100 ppm NO_2-containing flue gas (inset: particle diameter distribution), (e) cycled DFM with 500 ppm NO_2-containing flue gas and EDX (inset: enlarged image).

peaks under 500 ppm SO_2 conditions. Two characteristic S 2p signals at 163.2 eV and 172.4 eV were assigned to sulfide and sulfate species, respectively. Although only CaS was identified in the bulk phase by XRD, XPS analysis revealed that both sulfide and sulfate species were present on the surface in comparable proportions at lower SO_2 concentrations. Under 500 ppm SO_2 conditions, the surface was dominated by sulfide species, in agreement with the increased CaS content observed by XRD. In contrast, for the NO_2-treated DFM, no nitrogen species were detected on the surface after 10 cycles, suggesting that nitrogen-containing intermediates were fully decomposed or desorbed during the dry reforming process. This observation is consistent with both the elemental analysis and the absence of stable nitrogen-containing phases in the XRD results.

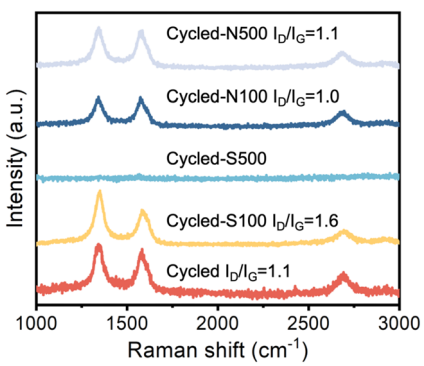

Fig. 12 Raman spectra of cycled DFMs.

Based on the above experimental findings, a mechanism is proposed to elucidate the influence of SO_2 and NO_2 on the ICCU-DRM process (Fig. 14). During the CO_2 capture stage, both SO_2 and NO_2 can be co-adsorbed by CaO alongside CO_2. The generated CaS and $CaSO_4$ species are thermally stable and persist into the subsequent CH_4 dry reforming stage, whereas calcium nitrates formed from NO_2 adsorption are thermodynamically unstable and decompose upon gas switching. The formation of CaS and $CaSO_4$ can act as physical barriers that suppress CaO sintering and thereby enhance the cyclic stability of the DFM. However, progressive accumulation of these sulfur species leads to the irreversible consumption of active CaO, reducing the theoretical CO_2 uptake capacity. In the case of NO_2, the decomposition of calcium nitrates during cycling may contribute to an improved pore structure, offering potential benefits for gas diffusion. During the CH_4 dry reforming stage, both SO_2 and NO_2 induce partial or total deactivation of the Ni active sites

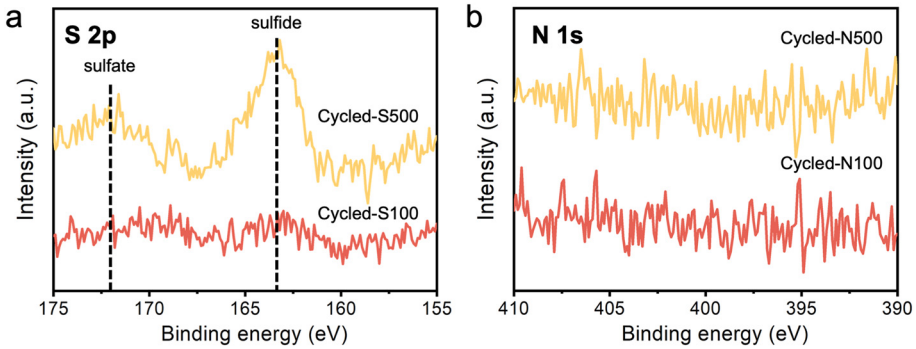

Fig. 13 XPS spectra of cycled DFMs. (a) SO_2-containing flue gas conditions and (b) NO_2-containing flue gas conditions.

through the formation of surface coating layers. NO_2 and low concentrations of SO_2 result in partial deactivation, leading to preserved CO_2 conversion but a notably reduced H_2 : CO ratio and suppressed carbon deposition. In contrast, high SO_2 concentrations cause near-complete deactivation of Ni sites, eliminating both CO and H_2 production. This mechanistic insight highlights the nuanced and concentration-dependent effects of flue gas pollutants on ICCU performance, providing important guidance for the development of sulfur- and nitrogen-tolerant DFM materials in realistic industrial applications.

3 Conclusions

In this study, we systematically evaluated the influence of SO_2 and NO_2 in flue gas on the ICCU-DRM performance and uncovered the relevant mechanism. Fixed-bed reactor results revealed that a low concentration of SO_2 (100 ppm) in flue gas showed a minor influence on the CO_2 conversion, but can effectively inhibit the methane decomposition side reactions, therefore significantly reducing the carbon deposition. Moreover, the low concentration of SO_2 in flue gas can effectively improve the stability of CO_2 capture. However, with the increase of SO_2 concentration to 500 ppm, the adsorption capacity and catalytic reforming capacity of the DFMs decreased significantly, and the materials were significantly deactivated after 10 cycles. NO_2 in flue gas exhibited a similar trend to SO_2 but at a lower impact level. Characterization studies revealed that both SO_2 and NO_2 induced a coating layer on the surface of Ni catalytic sites, which reduced the catalytic performance of the Ni active sites, and then affected the performance of the DFM. This study provided a solid foundation for the design and application of DFMs under realistic flue gas conditions.

4 Experimental section

4.1 Material synthesis

The typical Ni5Al15Ca DFM was synthesized by a sol–gel method. Calculated amounts of 15.11 g $Ca(NO_3)_2{\cdot}4H_2O$ (Aladdin, 99.9%), 4.50 g $Al(NO_3)_3{\cdot}9H_2O$ (Aladdin, 99.9%), and 1.16 g $Ni(NO_3)_2{\cdot}6H_2O$ (Aladdin, 99.9%) were dissolved in 60 mL deionized water and stirred for 1 h. 15.36 g citric acid (Aladdin, 99.5%) was then added to the solution with another

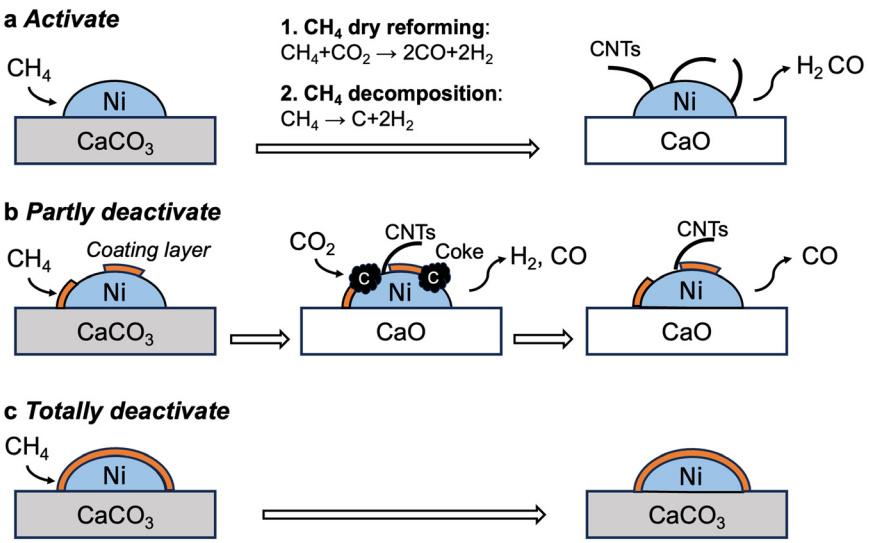

Fig. 14 Influence mechanism illustration of SO_2 or NO_2 pollutants in flue gas for ICCU-DRM.

1 h. Then the mixture was heated to 90 °C with an oil bath. The mixture formed a wet-gel after *ca.* 5 h, which was subsequently aged overnight in an oven at 120 °C to form a dry-gel. The dry-gel was then calcined in a muffle furnace at 850 °C for 2 h with a ramp rate of 10 °C min^{-1}. The as-synthesized powder was granulated to 40–60 mesh size. Finally, the Ni5Al15Ca DFM was pretreated in H_2 at 700 °C for 3 h.

4.2 Material characterization

The molar ratios of Ni, Al, Ca and S in the DFM were calculated using ICP-OES (Agilent ICPOES730) after digestion in nitric acid. The N element was analyzed using an elementary analyzer (EA, Thermo Scientific Flash Smart Analyzer). The crystal structure of the DFM was measured by XRD (PANalytical Empyrean series) equipped with a Bragg–Brentano high-definition mirror. The data were collected within the 2theta range of 10–90° with a step size of 0.01303° and 50 s per step. SEM (JEOL JSM-9700F) was applied to characterize the morphology and element distribution of the materials. The morphologies of nanoparticles and element distributions were investigated by TEM (JEOL JEM-2100 Plus, operated at 200 kV) equipped with EDX. The surface area and pore volume of the materials were determined by N_2 physisorption (Micromeritics, ASAP 2460 analyzer), with the Brunauer–Emmett–Teller (BET) model (using the adsorption data) and the Barrett–Joyner–Halenda (BJH) model (using the desorption data), respectively. XPS (SPECS) with an Al Kα X-ray source and a PHOIBOS 150 analyzer was performed for surface element analysis. The C 1s peak of adventitious carbon was set at 284.8 eV to correct for any charge-induced shifts. H_2-TPR (Micromeritics, AutoChem II-2920 system) was performed to evaluate the reducibility of the DFM. *Ca.* 100 mg sample was pretreated at 800 °C under an Ar atmosphere. After cooling to room temperature, the sample was reduced at a ramp rate of 10 °C min^{-1} under 10% H_2/Ar from room temperature to 1000 °C. The carbon capture capacity of the DFM was evaluated by TGA (NETZSCH STA2500). *Ca.* 5 mg sample was placed in an alumina pan in the analyzer chamber and the weight signal was collected at 650 °C under 15% CO_2/N_2.

4.3 Performance test of integrated carbon capture and methane dry reforming

The performance of integrated carbon capture and methane dry reforming (ICCU-DRM) was evaluated using a fixed-bed system. A gas analyzer (Cubic Ruiyi Instruments, Gasboard 3000) was used to analyzed the real-time concentration of gas. CO_2, CO and CH_4 were detected using a non-dispersive infrared (NDIR) detector, while H_2 was detected using a thermal conductivity detector (TCD). Briefly, *ca.* 200 mg DFM was placed in a quartz tube with an internal diameter of 8 mm. As for a typical ICCU-DRM test, the DFM was first pretreated under N_2 (50 mL min^{-1}) at 675 °C to remove the adsorbed CO_2. Subsequently, the carbon capture stage was performed under 15%CO_2/N_2 (50 mL min^{-1}) at 650 °C for 40 min. As for SO_2 and NO_2-containing flue gas, corresponding concentrations of SO_2 and NO_2 were mixed into the flue gas. The uncaptured CO_2 was purged with N_2 (50 mL min^{-1}) for 10 min. As for the dry reforming stage, the DFM was exposed to 10% CH_4/N_2 (50 mL min^{-1}) at 675 °C for 30 min, followed by purging with N_2 (50 mL min^{-1}) for 10 min. All working conditions were repeated for 10 capture/conversion cycles to test the stability of the DFM. All experiments were operated at atmospheric pressure.

The CO yield in the carbon capture stage, CO_2 uptake, CO_2 conversion, and H_2 : CO ratio were calculated as follows:

$$\text{CO yield in carbon capture stage } (\text{mmol g}^{-1}) = \frac{\int F^{\text{out}}_{\text{Cap,CO}}(t)\mathrm{d}t}{m_{\text{DFM}}}$$

$$\text{CO}_2 \text{ uptake } (\text{mmol g}^{-1}) = \frac{\int\left[F^{\text{in}}_{\text{Cap,CO}_2}(t) - F^{\text{out}}_{\text{Cap,CO}_2}(t) - F^{\text{out}}_{\text{Cap,CO}}(t)/2\right]\mathrm{d}t}{m_{\text{DFM}}}$$

$$\text{CO}_2 \text{ conversion } (\%) = \frac{\int F^{\text{out}}_{\text{Con,CO}}(t)/2\mathrm{d}t}{\int\left[F^{\text{out}}_{\text{Con,CO}}(t)/2 + F^{\text{out}}_{\text{Con,CO}_2}(t)\right]\mathrm{d}t}$$

$$\text{H}_2:\text{CO ratio } (1) = \frac{\int F^{\text{out}}_{\text{Con,H}_2}(t)\mathrm{d}t}{\int F^{\text{out}}_{\text{Con,CO}}(t)\mathrm{d}t}$$

where F denotes the molar flow rate of the gas, Cap and Con refer to the carbon capture stage and the conversion stage, and m_{DFM} represents the mass of the DFM.

4.4 *In situ* XRD

In situ XRD experiments were conducted on an XRD instrument (PANalytical, Empyrean Series) equipped with an XRK 900 reactor chamber from Anton Paar (Anton Paar, XRK-900). The DFMs were firstly *in situ* reduced at 700 °C under a flow of 100 mL min^{-1} H_2 for 1 h, followed by purging in N_2. Subsequently, 100 mL min^{-1} 2000 ppm SO_2/15% CO_2/N_2 was introduced into the chamber for 90 min. After another 100 mL min^{-1} N_2 purge, 100 mL min^{-1} 20% CH_4/N_2 was introduced into the chamber for 90 min. The XRD patterns were continuously recorded within the 2theta range of 20–45° with 2.5 min per scan.

Data availability

The data that support the findings of this study are available from the corresponding author upon reasonable request.

Author contributions

H. Z., S. S. and B. Y. conceived the research project. B. Y. designed the experimental work. B. Y., M. Y. and Y. W.

performed the experiments. B. Y. contributed to the *in situ* XRD experiments. Y. X. and X. B. assisted with the catalyst characterization. Data analysis and interpretation were discussed among all coauthors. B. Y., S. S. and H. Z. wrote the manuscript, with contributions from all authors.

Conflicts of interest

There are no conflicts to declare.

Acknowledgements

This work was supported by the National Key R&D Program of China (2023YFB4104000), the Beijing Natural Science Foundation (JQ24053), the National Natural Science Foundation of China (52276202), the Special support program for young talent innovation teams from Zhengzhou University (32320673), the Carbon Neutrality and Energy System Transformation (CNEST) project (2023YFE0204600), the International Joint Mission On Climate Change and Carbon Neutrality, and the Tsinghua University Initiative Scientific Research Program.

References

1 J. Rogelj, M. Den Elzen, N. Höhne, T. Fransen, H. Fekete, H. Winkler, R. Schaeffer, F. Sha, K. Riahi and M. Meinshausen, Paris Agreement climate proposals need a boost to keep warming well below 2 °C, *Nature*, 2016, **534**, 631–639.

2 Z. Liu, Z. Deng, G. He, H. Wang, X. Zhang, J. Lin, Y. Qi and X. Liang, Challenges and opportunities for carbon neutrality in China, *Nat. Rev. Earth Environ.*, 2021, **3**, 141–155.

3 Z. Zhang, S.-Y. Pan, H. Li, J. Cai, A. G. Olabi, E. J. Anthony and V. Manovic, Recent advances in carbon dioxide utilization, *Renewable Sustainable Energy Rev.*, 2020, **125**, 109799.

4 D. U. Nielsen, X.-M. Hu, K. Daasbjerg and T. Skrydstrup, Chemically and electrochemically catalysed conversion of CO_2 to CO with follow-up utilization to value-added chemicals, *Nat. Catal.*, 2018, **1**, 244–254.

5 W. Gao, S. Liang, R. Wang, Q. Jiang, Y. Zhang, Q. Zheng, B. Xie, C. Y. Toe, X. Zhu, J. Wang, L. Huang, Y. Gao, Z. Wang, C. Jo, Q. Wang, L. Wang, Y. Liu, B. Louis, J. Scott, A.-C. Roger, R. Amal, H. He and S.-E. Park, Industrial carbon dioxide capture and utilization: State of the art and future challenges, *Chem. Soc. Rev.*, 2020, **49**, 8584–8686.

6 Y. Wang, R. Li, C. Zeng, W. Sun, H. Fan, Q. Ma and T.-S. Zhao, Recent research progress of methane dry reforming to syngas, *Fuel*, 2025, **398**, 135535.

7 A. H. K. Owgi, A. A. Jalil, I. Hussain, N. S. Hassan, H. U. Hambali, T. J. Siang and D. V. N. Vo, Catalytic systems for enhanced carbon dioxide reforming of methane: A review, *Environ. Chem. Lett.*, 2021, **19**, 2157–2183.

8 H. McLaughlin, A. A. Littlefield, M. Menefee, A. Kinzer, T. Hull, B. K. Sovacool, M. D. Bazilian, J. Kim and S. Griffiths, Carbon capture utilization and storage in review: Sociotechnical implications for a carbon reliant world, *Renewable Sustainable Energy Rev.*, 2023, **177**, 113215.

9 T. M. Gür, Carbon dioxide emissions, capture, storage and utilization: Review of materials, processes and technologies, *Prog. Energy Combust. Sci.*, 2022, **89**, 100965.

10 J. Chen, Y. Xu, P. Liao, H. Wang and H. Zhou, Recent progress in integrated CO_2 capture and conversion process using dual function materials: A state-of-the-art review, *Carbon Capture Sci. Technol.*, 2022, **4**, 100052.

11 S. Sun, H. Sun, P. T. Williams and C. Wu, Recent advances in integrated CO_2 capture and utilization: A review, *Sustainable Energy Fuels*, 2021, **5**, 4546–4559.

12 S. Sun, B. Yu, Y. Shen, Y. Liu, H. Sun, X. Bie, M. Wu, Y. Xu, C. Wu and H. Zhou, Promoting proximity to enhance Fe-Ca interaction for efficient integrated CO_2 capture and hydrogenation, *Sep. Purif. Technol.*, 2025, **357**, 130227.

13 E. García-Bordejé, J. M. Conesa, A. Guerrero-Ruiz and I. Rodríguez-Ramos, Bifunctional Na–Ru on gamma-alumina for CO_2 capture from air and conversion to CH_4 : Impact of the regeneration method and support on monolithic contactors, *Ind. Chem. Mater.*, 2025, DOI: **10.1039. D5IM00030K**.

14 H. Liu, L. Cen, X. Xie, L. Liu, Z. Sun and Z. Sun, Engineering nanoparticle structure at synergistic Ru-Na interface for integrated CO_2 capture and hydrogenation, *J. Energy Chem.*, 2025, **100**, 779–791.

15 Y. Shen, S. Sun, H. Sun, Y. Xu, H. Zhou, C. Wu and H. Qiu, Dual functional materials for integrated CO_2 capture and utilization (ICCU): Design, fabrication, performances, and challenges, *Chem. Eng. J.*, 2025, **512**, 162440.

16 Z. Lv, C. Qin, S. Chen, D. P. Hanak and C. Wu, Efficient-and-stable CH_4 reforming with integrated CO_2 capture and utilization using Li_4SiO_4 sorbent, *Sep. Purif. Technol.*, 2021, **277**, 119476.

17 B. Shao, G. Hu, K. A. M. Alkebsi, G. Ye, X. Lin, W. Du, J. Hu, M. Wang, H. Liu and F. Qian, Heterojunction-redox catalysts of $Fe_xCo_yMg_{10}CaO$ for high-temperature CO_2 capture and in situ conversion in the context of green manufacturing, *Energy Environ. Sci.*, 2021, **14**, 2291–2301.

18 S. Bahrami Gharamaleki, S. Carrasco Ruiz, T. Ramirez Reina, M. Short and M. S. Duyar, Effect of adsorbent loading on NaNiRu-DFMs' CO_2 capture and methanation: Finding optimal Na-loading using Bayesian optimisation guided experiments, *Ind. Chem. Mater.*, 2025, DOI: **10.1039. D5IM00019J**.

19 S. Sun, Y. Wang, Y. Xu, H. Sun, X. Zhao, Y. Zhang, X. Yang, X. Bie, M. Wu, C. Zhang, Y. Zhu, Y. Xu, H. Zhou and C. Wu, Ni-functionalized Ca@Si yolk-shell nanoreactors for enhanced integrated CO_2 capture and dry reforming of methane via confined catalysis, *Appl. Catal., B*, 2024, **348**, 123838.

20 J. Hu, P. Hongmanorom, V. V. Galvita, Z. Li and S. Kawi, Bifunctional Ni-Ca based material for integrated CO_2 capture and conversion via calcium-looping dry reforming, *Appl. Catal., B*, 2021, **284**, 119734.

21 Y. Hu, H. Lu, W. Liu, Y. Yang and H. Li, Incorporation of CaO into inert supports for enhanced CO_2 capture: A review, *Chem. Eng. J.*, 2020, **396**, 125253.
22 H. Sun, C. Wu, B. Shen, X. Zhang, Y. Zhang and J. Huang, Progress in the development and application of CaO-based adsorbents for CO_2 capture—A review, *Mater. Today Sustain.*, 2018, **1–2**, 1–27.
23 Y. Hu, Q. Xu, X. Zou, X. Wang, H. Cheng, X. Zou and X. Lu, M_xO_y (M = Mg, Zr, La, Ce) modified Ni/CaO dual functional materials for combined CO_2 capture and hydrogenation, *Int. J. Hydrogen Energy*, 2023, **48**, 24871–24883.
24 Y. Guo, G. Wang, J. Yu, P. Huang, J. Sun, R. Wang, T. Wang and C. Zhao, Tailoring the performance of Ni-CaO dual function materials for integrated CO_2 capture and conversion by doping transition metal oxides, *Sep. Purif. Technol.*, 2023, **305**, 122455.
25 X. Xu, B. Yu, M. S. Hussain, Y. Wang, Q. Li, Y. Xu, Y. Zhang and H. Zhou, One-pot synthesis of cost-effective dual functional material from solid waste for integrated CO_2 capture and utilization, *Sep. Purif. Technol.*, 2025, **372**, 133309.
26 N. Pegios, G. Schroer, K. Rahimi, R. Palkovits and K. Simeonov, Design of modular Ni-foam based catalysts for dry reforming of methane, *Catal. Sci. Technol.*, 2016, **6**, 6372–6380.
27 E. Wang, Z. Zhu, R. Li, J. Wu, K. Ma and J. Zhang, Ni/CaO-based dual-functional materials for calcium-looping CO_2 capture and dry reforming of methane: Progress and challenges, *Chem. Eng. J.*, 2024, **482**, 148476.
28 S. Jo and K. L. Gilliard-AbdulAziz, Self-regenerative Ni-doped $CaTiO_3$ /CaO for integrated CO_2 capture and dry reforming of methane, *Small*, 2024, 2401156.
29 Y. Zhao, R. Hao, T. Wang and C. Yang, Follow-up research for integrative process of pre-oxidation and post-absorption cleaning flue gas: Absorption of NO_2, NO and SO_2, *Chem. Eng. J.*, 2015, **273**, 55–65.
30 X. Zhou, H. Yi, X. Tang, H. Deng and H. Liu, Thermodynamics for the adsorption of SO_2, NO and CO_2 from flue gas on activated carbon fiber, *Chem. Eng. J.*, 2012, **200–202**, 399–404.
31 R. Chen, T. Zhang, Y. Guo, J. Wang, J. Wei and Q. Yu, Recent advances in simultaneous removal of SO_2 and NO_x from exhaust gases: Removal process, mechanism and kinetics, *Chem. Eng. J.*, 2021, **420**, 127588.
32 A. Bhaskaran and S. Roy, Exploring dry reforming of CH_4 to syngas using high-entropy materials: A novel emerging approach, *ChemCatChem*, 2025, **17**, e202401297.
33 T. Y. Yeo, J. Ashok and S. Kawi, Recent developments in sulphur-resilient catalytic systems for syngas production, *Renewable Sustainable Energy Rev.*, 2019, **100**, 52–70.
34 H. Li, X. Peng, M. An, J. Zhang, Y. Cao and W. Liu, Negative effect of SO_2 on mercury removal over catalyst/sorbent from coal-fired flue gas and its coping strategies: A review, *Chem. Eng. J.*, 2023, **455**, 140751.
35 H. Yu, C. Shan, J. Li, X. Hou and L. Yang, Alkaline absorbents for SO_2 and SO_3 removal: A comprehensive review, *J. Environ. Manage.*, 2024, **366**, 121532.
36 N. Ding, Y. Zheng, C. Luo, Q. Wu, P. Fu and C. Zheng, Development and performance of binder-supported $CaSO_4$ oxygen carriers for chemical looping combustion, *Chem. Eng. J.*, 2011, **171**, 1018–1026.